MANSOURA JOURNAL OF CHEMISTRY
Official Journal of Faculty of Science, Mansoura University, Egypt
E-mail: scimag@mans.edu.eg ISSN: 2974-4938

Fabrication of nanotitania/calcium alginate and cupper ferrite/calcium alginate nanocomposite beads: adsorption of methylene blue

Asaad F. Hassan [a], *, *Gehan A. El-Naggar* [a], *Amany G. Braish* [a], *Maha S. Elsayed* [b], *Mona M. Abd El-Latif* [c]

[a] *Chemistry Department, Faculty of Science, Damanhour University, Damanhour 22511, Egypt.*

[b] *Central Laboratory of Date Palm Research and Development, Agricultural Research Center, Giza 12619, Egypt.*

[c] *Advanced Technology and New Materials Research Institute, City of Scientific Research and Technological Applications, Alexandria 21934, Egypt.*

* ***Corresponding Author***: *Prof. Dr. Asaad F. HassanEmail: asmz68@sci.dmu.edu.eg, Tel: 01005105504.*

Received:5//10/2022
Accepted: 1/11/2022

Abstract: In this study five solid adsorbents nanoparticles were synthetized namely: titanium dioxide (NT), calcium alginate (AG), cupper ferrite (CF), cupper ferrite/calcium alginate composite (CG), and titanium dioxide/calcium alginate composite (TG). The fabricated materials were investigated by different tools such as loss on drying, TGA, N_2 adsorption/desorption, XRD, SEM, TEM, pH_{PZC}, and FTIR. These synthetized materials were used as solid adsorbents for methylene blue adsorption under different conditions. The characterization tools prove that TG nanoparticles is characterized by 361.1 m^2/g (specific surface area), 4.51 nm (pore radius), 5.80 (pH_{PZC}), nearly 90 nm (TEM particle size), and the presence of many polar chemical functional groups. TG showed the maximum Langmuir adsorption capacity at 40 ^oC (448.76 mg/g) with obeying of PFO, Elovich kinetic model, spontaneous, endothermic, and physical adsorption process as reported by kinetic and thermodynamic studies. Adsorption of MB onto all the investigated solid materials follows Freundlich, Temkin, Dubinin-Radushkevich, and Langmuir adsorption models with correlation coefficients > 0.9242. Desorption studies prove that ethanol is the most accepted desorbing solution with 75.46% desorption efficiency.

keywords: Nanotitania; alginate; cupper ferrite; methylene blue; adsorption.

1.Introduction

Freshwater is not sufficient enough to satisfy the demands of the existing and growing population. Water shortage is considered as a major problem in the present world, which is not only represented a decrease in the suitable water resources, but also related to polluted sources of water. Day by day the amount of harmful organic dyes released into water bodies is growing as a result of industries and human activity which leads to dye accumulation in wastewater which is considered as one of the major sources of pollution in the world wide. Dyes have an essential role in our life, based on their applications in industries like tanning of leather, pharmaceuticals, textile, food, medicine, agricultural, paper production, color photography, hair coloring, cosmetic, rubber, plastics, wood staining, and photo electrochemical cells [1,2]. The major portion of dyes is lost during their preparation and application which rejected in wastewater [3]. Dyes are found to resist the common reduction and oxidation process and difficult to remove from different industrial waste due to resistance of anaerobic/aerobic digestions, stable towards heat and light, as well as biodegradation [4–6]. Most synthetic dyes have mutagenic effects, carcinogenic, and toxic on living organisms [7]. Methylene blue dye (MB) is a common basic cationic dye with a high adsorption ability, low price, and wide availability [8]. MB has different toxic effects, include tissue necrosis, breathing difficulties, vomiting, nausea, heart rate increasing, mental confusion, permanent injury to the eyes gastritis, painful, convulsions, dyspnea, skin sensitivity, tachycardia in humans, and methemoglobinemia like syndromes [9–12]. Different techniques are devoted to remove these toxic dyes from water such as sedimentation, chemical precipitation, filtration, magnetic fields, fluidized bed reactor, ion flotation, coagulation/flocculation, anaerobic/aerobic treatment, electro kinetic coagulation, sonochemical degradation, ozonation, irradiation, electrochemical degradation, reverse osmosis, flue gas purification, membrane electrolysis, evaporation, aeration screening, straining, sedimentation, disinfection, fluoridation, oxidation, fungal decolonization, biological membranes, and ion-exchange processes [13–16]. Adsorption is considered as the most favorable used physical process, because of its ease of application, presence of different solid adsorbents, there is no need for a large application area, economic cost due to the reusability of solid adsorbent, high efficiency even at low concentrations, shorter operational duration, and negligible production of toxic byproducts [17–20]. In procedures to remove dyes from water, a wide range of natural or synthesized inorganic materials have been utilized as adsorbent materials. These materials have varied structural, chemical, and surface properties.

Nanomaterials have unique surface properties such as a huge surface area, large number of grain boundaries, small size, surface free energy, reactivity, sorption efficiency, low temperature modification, and short intra-particle diffusion distance [21,22]. Nanomaterials have been used in the process of adsorption such as inorganic nanoparticles (metal oxide and metal), nanomaterials of carbon (graphene, multi-walled nanotubes, single-walled nanotubes, fullerene), and nanoparticles of polymer compounds. Titanium dioxide nanoparticles is considered as one of the most suitable solid adsorbent that used in the removal of many toxic pollutants due to its biocompatibility, chemical stability, low cost, and non-toxicity. Also, cupper ferrite is one of the most preferable materials used as magnetic biosorbents. Titania is widely used in different fields as adsorption, photocatalysis, catalysis, and in electromagnetic and spintronic devices [23–25]. Nevertheless, nanoparticles of metal or metal oxides tend to aggregate due to the higher surface free energy and weak Van der Waals forces [26]. The aggregation of nanoparticles takes part in the reduction of surface area and mechanical properties change of nanoparticles which is not accepted in the process of adsorption. Hence, magnetic adsorbents have been prepared by the combination between those nanoparticles with biopolymer adsorbent like alginate (composite) which in turn improves the dispersion and reusability of the new formed composite.

In the present work calcium alginate (AG), titanium dioxide (NT), cupper ferrite (CF), titanium dioxide/calcium alginate composite (TG), and cupper ferrite/calcium alginate composite (CG) nanoparticles were prepared. The prepared nanoparticles were characterized by various methods such as: loss on drying, TGA, XRD, TEM, SEM, point of zero charge, nitrogen adsorption, and FTIR. Adsorption of methylene blue (MB) dye was carried out under optimum conditions as effect of adsorbent dosage, pH of initial solution, time, temperature, and initial dye concentration. Desorption of MB was studied to evaluate solid adsorbent reusability.

2. Materials and methods

2.1 Materials

Titanium isopropoxide (97%), cupper nitrate trihydrate (99%), and ferric nitrate nonahydrate (≥ 99.95%) were obtained from Chema Tec Co., Egypt. Sodium alginate, calcium chloride (≥ 97%), isopropanol (70%), and methylene blue were supplied by Sigma-Aldrich. Sodium chloride, propanol, ethanol (96%), benzene, chloroform (99.5%), NaOH (≥ 98%), and HCl (37%) were supplied by El-Nasr for Pharmaceutical and Chemical Industrial Co., Egypt.

2.2. Solid adsorbents preparation

2.2.1. Synthesis of calcium alginate (AG)

Sodium alginate (1%) and $CaCl_2$ (3%) solutions were separately prepared in distilled water. Solution of sodium alginate was added drop by drop to the prepared solution of $CaCl_2$. The added solution of sodium alginate was transformed to calcium alginate beads that were insoluble in water. All beads were then washed many times with distilled water to eliminate any residual $CaCl_2$ from the surface. The obtained beads were then dried for 12 h at 70° C [9].

2.2.2. Synthesis of titanium dioxide nanoparticles (NT)

Sol–gel method was used to prepare titanium dioxide nanoparticles. Mixture of 15 mL titanium isopropoxide and 60 mL isopropanol was subjected to vigorous stirring. Isopropanol/HCl/H_2O (1:100:50) solution was added drop-by-drop to the previous solution with constant stirring. The formed gel was removed by centrifugation and dried at 110° C in an oven before being calcined for 3 h at 500° C in a muffle [27].

2.2.3. Synthesis of cupper ferrite nanoparticles (CF)

0.025 mol $Cu(NO_3)_2.3H_2O$ and 0.05 mol $Fe(NO_3)_3.9H_2O$ in 100 mL distilled water were mixed and the resultant mixture was added to 75 mL of 4M NaOH solution. The formed precipitate was heated at 90° C for 2 h, filtered off, washed by distilled water, and dried at 80° C overnight [28].

2.2.4. Synthesis of titanium dioxide/calcium alginate composite (TG)

Sodium alginate solution 2% (w/v) was stirred to obtain homogeneous solution. Under constant stirring for 2 h, 50 mL of the prepared sodium alginate (2% w/v) was mixed with 1.25 g titanium dioxide nanoparticles (NT). The mixture (titanium dioxide/sodium alginate mixture) was added dropwise onto aqueous $CaCl_2$ solution (100 mL, 2 g/L) with continuous stirring. The formed beads were kept for 2 h in its mother liquor. Finally, the beads were collected using dry filter paper, rinsed multiple times with distilled water, and drying overnight at 80° C [29].

2.2.5. Synthesis of cupper ferrite/calcium alginate composite (CG)

Two percent solution (w/v) of sodium alginate was stirred for 24 h to get a homogeneous solution. After that, 50 mL of sodium alginate solution was mixed with 1.25 g of cupper ferrite nanoparticles (CF) under constant stirring. The previous mixture was introduced dropwise into solution of $CaCl_2$ (100 mL, 2 g/L) under continuous stirring. The formed beads were kept in a solution of $CaCl_2$ for 2 h. The formed beads were collected by filtration using filter paper followed by washing with distilled water, and dried for 24 h at 80° C.

2.3. Characterization of the synthesized materials

Thermal degradation of AG, NT, CF, TG, and CG was investigated using SDT Q600 V20.9 Build 20 instrument, UK (differential thermal analyzer) at a N_2 gas flow rate of 40 mL/min with heating rate of 10 °C/min till 800 °C.

During drying the weight loss for all samples was calculated by using 0.5 g of the sample in crucible and put it at 110 °C for 24 h, till constant weight.

$$\%\text{Weight loss on drying} = \frac{W_b - W_a}{W_b} \times 100 \quad (1)$$

Where W_a and W_b are the weight of sample after and before drying, respectively.

Based on N_2 adsorption experiment, S_{BET} (specific surface area, m^2/g), V_p (total pore volume, mL/g), and $\bar{r}$ (average pore radius, nm) were determined at –196 °C using gas sorption analyzer (NOVA 3200e, Quantachrome Corporation, USA).

The textural structure of the samples was examined by using SEM (scanning electron microscopy), JEOL JSM-6510LV model, Japan. Adsorbent particles morphology was also investigated using TEM (transmission electron microscopy), JEOL-JEM-2100 model, Japan.

Phase identification of a crystalline material is determined by X-ray diffraction. The samples were ground and pushed into the sampler cell and studied with X-ray diffractometer operating at 40 mA and 40 kV and secondary monochromator. All database was presented in the 2θ range at start position 5° up to 80°, with a scanning step at 2θ of 0.5°/ min. The average crystalline sizes (*D*) of the prepared adsorbents were evaluated from Debye-Scherrer equation (Eq. 2) while, the crystallinity (*Xc*) was estimated by equation (3) [30].

$$D = \frac{K\lambda}{\beta_{1/2}\cos\theta} \quad (2)$$

$$X_c = \left(\frac{K_A}{\beta_{1/2}}\right)^3 \quad (3)$$

Where K is dimensionless shape factor with a value equal to 0.9, λ is the X–ray wavelength, $\beta_{1/2}$ represents the full width at half maximum of peaks, θ is related to the diffraction angle, and K_A is a constant (0.24).

The Fourier transform infrared spectra of the powders in the range of 4000–400 cm^{-1} were recorded using Mattson 5000 FTIR spectrometer, USA. The samples were prepared using a small amount (~15 mg) and mixed with 25 to 30 times from its KBr volume in an agate mortar. The sample was pressed at 3500 kg/cm^2 for 5 min. The prepared disc was introduced into Nic-Plan FTIR microscope, with a resolution of 6 cm^{-1} at 30 scans, and followed by deleting the background at the same settings.

pH_{PZC} (point of zero charge) was carried out by; 50 mL of NaCl (0.1 mol/L) were placed into flasks. The acidity within flasks was adjusted in a certain pH range (2–10) by the addition of either HCl (0.1 mol/L) and/or NaOH (0.1 mol/L). Portion of the prepared solid (0.1 g) was mixed with each flask, the flasks were shaken for overnight. The equilibrium pH value (pH_{final}) was then measured. The pH_{PZC} is the pH of the equilibrium solution at which the net surface charge measures zero ($pH_{final} - pH_{initial}$ = zero) [31].

2.4. Adsorption studies

50 mL of MB (300 mg/L) at the desired pH were taken in 250 mL Erlenmeyer flasks. Known amount of adsorbents were added to the investigated solution of adsorbate and was shaken for 24 hr. The supernatant liquid was then filtered off by using Whatman filter paper (Grade1). Then, the remaining unadsorbed molecules from MB solution (C_e, mg/L) was determined by UV-visible spectrophotometer at 663 nm. The percent removal of dyes and equilibrium adsorption capacity, (q_e, mg/g), were calculated by the following relationships, respectively [32]:

$$R\,(\%) = \frac{C_o - C_e}{C_o} \times 100 \quad (4)$$

$$q_e = \frac{C_o - C_e}{m} \times V$$

of adsorption/desorption rates (L/mg). R_L (dimensionless separation factor) is calculated to explain the nature of MB adsorption. If R_L > 1 (unfavorable adsorption), if 0 < R_L < 1 (favorable adsorption), and R_L = 0 (reversible adsorption).

$$R_L = \frac{1}{(1 + b\,C_0)} \quad (12)$$

The Freundlich isotherm model **(**Eq. 13**)** is expressed linearly as [38]:

$$\mathrm{Ln}\, q_e = \mathrm{Ln}\, K_f + \frac{1}{n}\, \mathrm{Ln}\, C_e \quad (13)$$

Where K_f (L/mg) is the Freundlich constant and n is related to the adsorption intensity.

The Temkin isotherm model studies the impact of several indirect adsorbate/adsorbent interactions. Temkin discovered that as coverage increased, adsorption heats tended to decrease, and is given by [39]

$$q_e = \beta_T\, \mathrm{Ln}\, K_T + \beta_T\, \mathrm{Ln}\, C_e \quad (14)$$

$$\beta_T = \frac{R\,T}{b_T} \quad (15)$$

Herein β_T represents on the heat of adsorption, K_T (L/g) is the equilibrium binding constant, T is the absolute adsorption temperature (°K), R (8.314 $J.mol^{-1}$. K^{-1}) is the universal constant of gas, while b_T is Temkin constant (J/mol).

The Dubinin−Radushkevich isotherm model is represented in a linear form by [40]

$$\mathrm{Ln}\, q_e = \mathrm{Ln}\, q_{DR} - K_{DR}\, \varepsilon^2 \quad (16)$$

$$\varepsilon = RT\mathrm{Ln}\left(1 + \frac{1}{C_e}\right) \quad (17)$$

Where K_{DR} (mol^2 kJ^{-2}) is a constant related to the mean adsorption energy, q_{DR} (mg/g) is the sorption capacity, and Polanyi potential is presented by ε. The mean free energy of adsorption (E_{DR}, kJ/mol) can also be worked out using the following equation:

$$E_{DR} = \frac{1}{\sqrt{2K_{DR}}} \quad (18)$$

2.7. Thermodynamic studies

The parameters of thermodynamic that used to determine the adsorption processes are $\Delta H°$ (change in enthalpy, kJ/mol), $\Delta S°$ (change in entropy, kJ/mol.K), and $\Delta G°$ (Gibb's free energy, kJ/mol), and these parameters were estimated by using the following models [41]:

$$K = \frac{C_s}{C_e} \quad (19)$$

$$\mathrm{Ln}\, K = \frac{\Delta S°}{R} - \frac{-\Delta H°}{RT} \quad (20)$$

$$\Delta G° = \Delta H° - T\,\Delta S° \quad (21)$$

Where, C_s, C_e, and R are related to the concentration of dye on solid, equilibrium concentration, and universal ideal gas constant, respectively. T is Kelvin temperature (°K).

2.8. Methylene blue desorption

Desorption study was conducted by weighing 0.5 g of TG pre-saturated with MB and mixed with 150 mL of pure desorbing solution (distilled water, propanol, benzene, ethanol, and chloroform) at ambient temperature for 12 h. The released concentration of MB was estimated in the solution by using a UV-vis spectrophotometer and desorption% was estimated using the following equation [42]:

$$\text{Desorption efficiency (\%)} = \frac{C_d \times V}{q \times W} \quad (22)$$

Herein C_d is related to the MB equilibrium concentration after the process of desorption from TG (mg/L), W (g) is the solid adsorbent mass, V (L) is the desorbing agent volume, and q (mg/g) is the maximum adsorption capacity of TG adsorbent.

3. Results and Discussion

3.1. Solid nanoparticles characterization

Thermal characterization includes thermogravimetric analysis (TGA) and weight loss on drying. NT showed the smallest percentage of loss on drying when compared with other samples which also confirmed by TGA analysis and modification with alginate leads to the increase in loss in drying Table (1). CG and TG give the highest values of weight loss during drying due to their higher water adsorption capacity as they have the highest specific surface area, as calculated from the data reported by nitrogen adsorption, compared with the others. TGA for AG, NT, CF, TG, and CG are shown in Fig. (1). AG graph could be separated into three thermal dissociation stages. At the first stage, mass loss (about 14%) from 20–200^o C which are related to the removal of surface adsorbed water molecules. The average weight loss 34% in the second stage is related to bond cleavage and chains dissociation with decarboxylation or dehydroxylation of the chain of polymer in the range between 200 and 450 ^{o}C [43]. The last period of thermal decomposition can be assigned to the decomposition process of polymer which resulted in pyrolysis from 450–800 ^{o}C with an average weight loss of about 72% at 675^o C [44]. While, thermal degradation of solid nanotitania (NT) presents a tiny mass loss (~ 6%) in the range 150–450^o C which is related to the decomposition of organic compounds occluded in TiO_2 during the preparation steps indicating its thermal stability [45]. Cupper ferrite nanoparticles continuously lose weight until 450 °C with 53% as a total loss. It may be related to the evaporation of adsorbed water and thermal dissociation of Fe and Cu hydroxides. Thermogravimetric curve shows a higher mass loss for nanotitania or cupper ferrite modified alginate (TG or CG, respectively) compared with the unmodified one (NT, CF) where modification raises the efficiency for absorption of water molecules. At 700 ^{o}C, TG exhibited a weight loss nearly 6.5 times more than that recorded by NT as its main single constituents (65 and 10% for TG and NT, respectively) while CG recorded 1.2 times more than CF (67 and 59% for CG and CF, respectively). Furthermore, the first weight losses for the composites were shifted to higher values, indicating a good interaction between ferrite, nanotitania, and alginate [46].

The specific surface area (S_{BET}, m^2/g), average pore radius ($\bar{r}$, nm), and total pore volume (V_T, cm^3/g) are listed in Table (1). The adsorption isotherms of nitrogen for all samples (AG, NT, CF, NT, and CG) are shown in Fig. (1). Based on the IUPAC classification, adsorption isotherm for AG and NT samples similar to type II adsorption isotherm with no hysteresis loop while CF, TG, and CG showed type IV with H1 hysteresis loop for pure CF and type H3 for TG and CG. Regarding the data in Table (1), S_{BET} and V_T of TG > CG > CF > NT > AG indicate the higher porosity of TG and CG nanocomposites and proving their higher adsorption capacity. The average pore radius ($\bar{r}$, nm) for TG (4.51 nm), CG (4.26 nm), and CF (2.97 nm) indicates the mesoporosity of the formed solid due to aggregation of nanoparticles while the average pore radius for NT (0.99 nm) and AG (0.91 nm) indicates the microporosity of solid [47].

AG powder is shown as single particles but in case of TG and CG, the aggregation confirmed the formation of composites. Moreover, the surface of the composites is much rougher, jagged, and uneven than that for pure alginate owing to modification and composite formation and that is evident a pore development of composites. The micrograph showed agglomerates of cupper ferrite nanoparticles and this may be due to the super para magnetism of nanoparticles. In the case of NT, clear wall boundaries can be observed.

TEM micrographs of the fabricated solids show sample particle sizes at the nanoscale. Comparing relative micrographs of the several figures reveal some notable variations in the size and morphology of particles. The histogram of TEM Fig. (2) revealed that 60% of AG particles present in the range of 100–125 nm while in the case of CF nearly 51% of the particles are located in the particle size range of 25–45 nm. The maximum observed NT particle size range (46%) are presented in the range of 50–75 nm. After composite formation TG and CG showed 55 and 42% of the particle sizes located in the range of 80–100 and 75–100 nm, respectively as alginate (AG) could have possibly accelerated nanotitania and cupper ferrite crystal nuclear growth.

Figure (1) exhibits XRD for all the synthetized solids where all the peaks are sharp revealing that the synthesized samples have high crystallinity and nano-sized particles, resulting in its high S_{BET} which agreed with SEM and nitrogen gas adsorption results. The displayed diffraction peaks at 2θ values of 13.5º, 20.47º, and 31.7º were observed for AG and related to the reflection of their (200) plane from polymannuronate, (110) plane from polyguluronate unit, and the other due to the amorphous halo [48]. XRD for NT detected different crystalline peaks are related to pure NT at nearly 2θ of 25.1º, 36.0º, 47.9º, 54.3º, 56.5º, 62.7º, and 64.1º, belong to the structure of anatase with (101), (004), (200), (105), (211), (204), and (116) planes, respectively [49] indicating the existence of predominant anatase phase, however, small peaks are detected at 2θ of 27.3º and 41.1º owing to the existence of small proportion of rutile phase [50]. The results conclude the successful formation of CF nanoparticle with no impurities in its structure [51]. The spectra of TG prove that the interactions between alginate and TiO_2 are Van der Waals forces and it is weaker than those between the molecules of alginate [52]. The crystallinity (X_c) was calculated from the diffraction peak broadening using Eq. 3 where the obtained data are shown in Table (1), revealing that AG, NT, CF, TG, and CG crystallinity (X_c) are about 1.2072, 3.9089, 2.4762, 1.6336, and 12.7376, respectively. The sizes of the crystallites in CF were 0.5341 nm; they grew to 1.2790 nm for the modified sample (CG) [53]. Since the presence of the modifiers accelerates CF crystallization and increases the crystallite sizes. The decrease in TG crystallite size may be related to AG segregation at the boundary of solid material [54]. All the above characters indicate successful coating of alginate onto the surface of NT and CF and good uniformity between the two phases.

According to data given in Table (1), the calculated point of zero charge (pH_{PZC}) values for AG, NT, CF, TG, and CG are 6.04, 4.40, 8.60, 5.80, and 6.70, respectively.

FTIR spectra for AG, NT, CF, TG, and CG are shown in Fig. (1). The observed band for AG at spectra with wavenumber range 3447 cm^{-1} can be assigned to –OH stretching due to phenolic groups [55]. The peaks for symmetric and asymmetric stretching of the carboxyl group were observed at 1419 and 1626 cm^{-1}, respectively. The characteristic peaks at 892.15 and 725.09 cm^{-1} which indicate the presence of mannuronic and guluronic fingerprint groups [56]. For nanotitania (NT), the peaks at 424 to 1078 cm^{-1} were assigned for Ti–O and O–Ti–O vibrations of pure titania [57]. The peak intensity at 424 to 1078 cm^{-1} is increased due to the stretching vibration of Ti–O–Ti. Some less intense peaks at 1992 to 2427 cm^{-1} indicating residual occluded organics within TiO_2 post the process of calcination [52]. The peak of CF at 598 cm^{-1} indicates the stretching vibration of Fe–O. The band around 600 cm^{-1} belongs the spinel ferrite's tetrahedral while the octahedral sites are related to the peak under 510 cm^{-1} [58]. TG showed characteristic peak located at 583 cm^{-1} proved the presence of titanium oxide nanoparticles in the composite [59]. The spectra showed a weak peak at nearly 1623 cm^{-1} and a strong peak at 620 cm^{-1}, which can be assigned to the O–H bending vibration of molecular H_2O or hydroxyls and deformation of TiO_4 tetrahedral [60]. While in case of CG, it was observed that the structure remains unchanged with the decrease in the intensity of peaks and slight shift in bands**,** confirmed the presence of $CuFe_2O_4$ in the network of alginate. Peaks at 500-880 cm^{-1} belong to O–Fe–O, Fe–O, and Fe–O–Fe lattice vibrations. The peaks under 500 cm^{-1} are related to the bond vibration of Cu–O.

Table (1): Textural parameters for AG, NT, CF, TG, and CG obtained from N_2 adsorption at –196 ^{o}C.

Sample	pH_{PZC}	Weight losson drying (%)	S_{BET} (m^2/g)	$\bar{r}$ (nm)	V_T (cm^3/g)	D (nm)	X_c
AG	6.04	5.9	65.3	0.91	0.02945	0.5983	1.2072
NT	4.40	1.6	87.1	0.99	0.04309	0.6107	3.9089
CF	8.60	4.7	110.5	2.97	0.16431	0.5341	2.4762
TG	5.80	5.1	361.1	4.51	0.81375	0.4278	1.6336
CG	6.70	6.2	165.3	4.26	0.35185	1.2790	12.7376

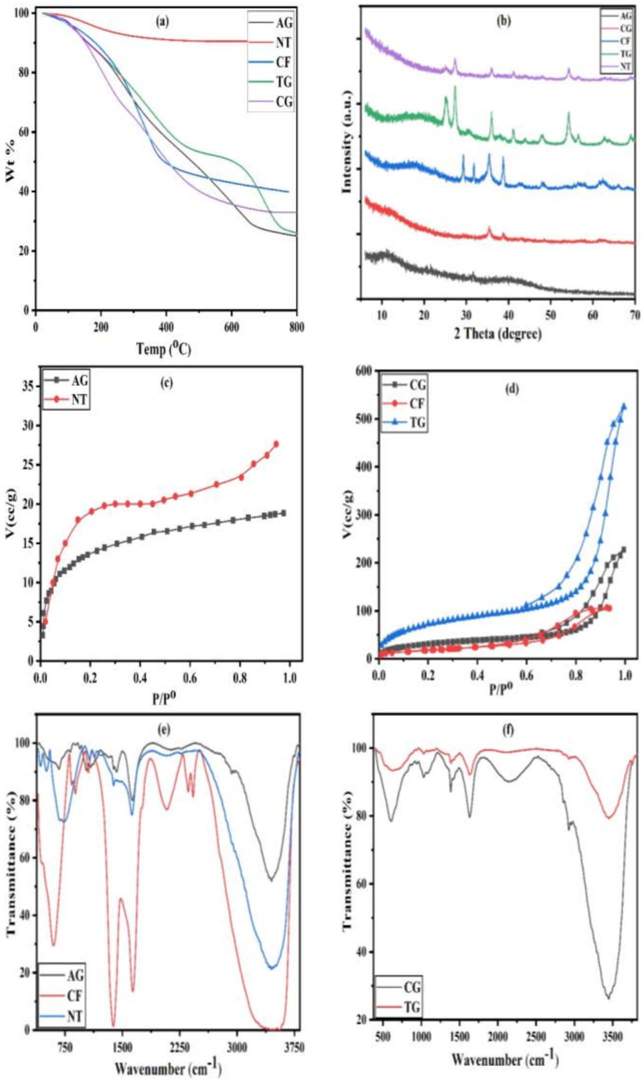

Fig. (1): (a) TGA curves, (b) XRD, (c, d) N_2 adsorption/desorption isotherms, and (e, f) FTIR of AG, NT, CF, TG, and CG.

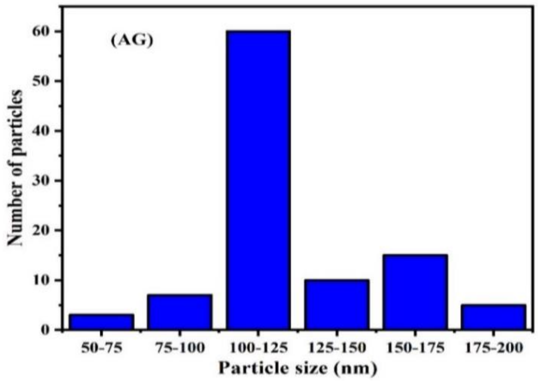

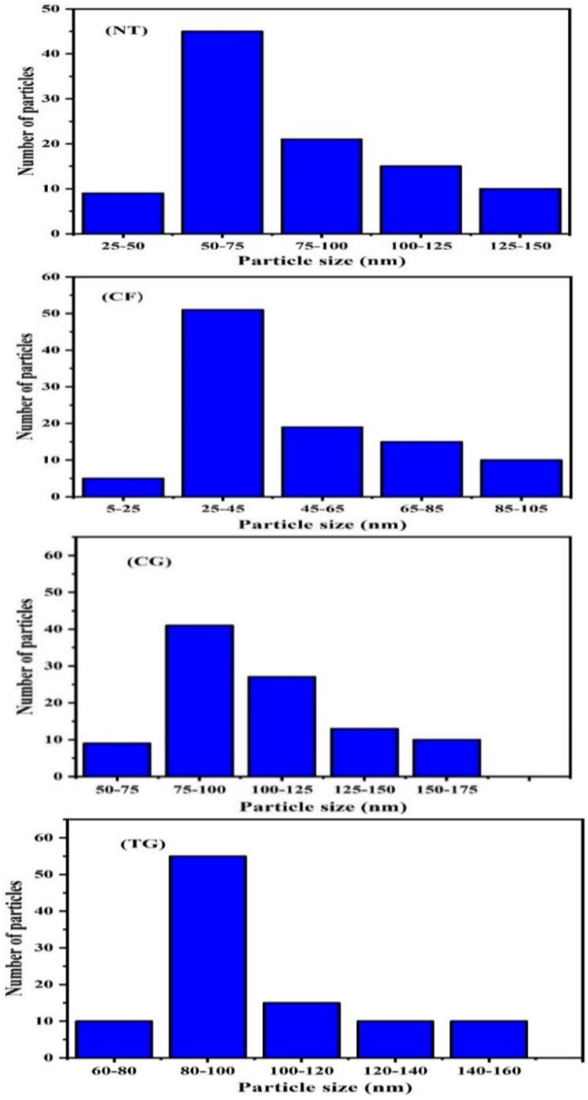

Fig. (2): Histograms obtained from TEM images for AG, NT, CF, TG, and CG.

3.2. Methylene blue adsorption

3.2.1. pH effect

pH plays an important factor in the adsorption of dye where it can affect the surface charge of solid adsorbent, functional groups dissociation of the active sites, can depress or promote the dye ionization [61]. The pH influence on adsorption process of MB dye onto AG, TG, and CG was carried out in pH values ranged between 2 and 12 at 17 °C as shown in Fig. (3a) and the removal% of MB was calculated by using Eq. 4. It is observed that at lower values of pH, the removal of methylene blue is low due to H^+ competition with MB^+ for the surface active sites of solid materials and increases with the increase in pH of adsorption solution due to the increase in the electrostatic interaction between the positively charged dye and the negatively surface of adsorbents [62]. Considering the pH_{PZC} values (6.04, 5.80, and 6.70) for the prepared solid samples (AG, TG, and CG, respectively), the surface of adsorbent will get positive charges at pH value < pH_{PZC} and negative charges at pH value > pH_{PZC}. The maximum removal of methylene blue is observed at pH8, where the calculated adsorption efficiency reaches 89.2, 97.5, and 95.1% for AG, TG, and CG, respectively.

3.2.2. Adsorbent dosage effect

Figure (3b) exhibits adsorbent dosage effect starting from 0.2 up to 2.0 g/L, while Eq. 4 was used to calculate the removal% of MB. It was observed that the removal percentage of MB increases with adsorbent dosage as the number of active sites for adsorption and S_{BET} (m^2/g) increase. The removal percentage of MB from aqueous solution increases rapidly up to 91.2, 95.2, and 93.2% for a dose of 1.4 g/L for AG, TG, and CG, respectively. At higher adsorbent dose (> 1.4 g/L), the adsorption reached the saturation state and there is no observable increase in MB removal. Based on the previous results we concluded that 1.4 g/L as adsorbent dosage was chosen as the optimum condition for adsorption of MB onto AG, TG, and CG.

3.2.3. Contact time effect

The effect of contact shaking time on MB adsorption onto AG, TG, and CG was carried out at 30 ^oC as shown in Fig. (3c). The adsorption of MB on the investigated solid adsorbents increased rapidly with the increase in time due to the increase in active sites on the adsorbents and then became slower until the equilibrium was reached in approximately 15 h due to saturation of active sites [63]. Figure (3d, e) shows PFO (Eq. 7) and Elovich (Eq. 10) linear plots while PSO (Eq. 8) and intra-particle diffusion (Eq. 9) linear plot. The parameters of kinetic model for the adsorption of MB on the investigated solids are listed in Table (2). Based on the results in Table (2), (i) pseudo-first order kinetic model was predominant as q_{exp} are closer to the experimental one (q_m) which obtained from Langmuir equation (3.4, 7.1, and 2.1% as differences in the case of AG, CG, and TG, respectively) and higher correlation coefficient (R^2) lies between 0.9818 and 0.9180. (ii) PSO cannot be accepted model for the adsorption of MB dyes onto the investigated solid nanoparticles because of the large differences between the calculated q_{exp} (calculated from kinetic procedures) and the experimental Langmuir values. (iii) The higher correlation coefficient values (0.8900–0.9517) indicate a good applicability of intra-particle diffusion model and it is not the rate limiting step but considered as a part from the adsorption process. (iv) The correlation coefficients of Elovich kinetic model were found to be (0.8966–0.9624) and indicating the good applicability of this model. Also, α and β values for the adsorption of MB onto AG, CG, and TG in the range of 116.8−194.5 mg/g.h and 0.0085−0.0228 g/mg, respectively and indicating the rapid surface coverage process [64].

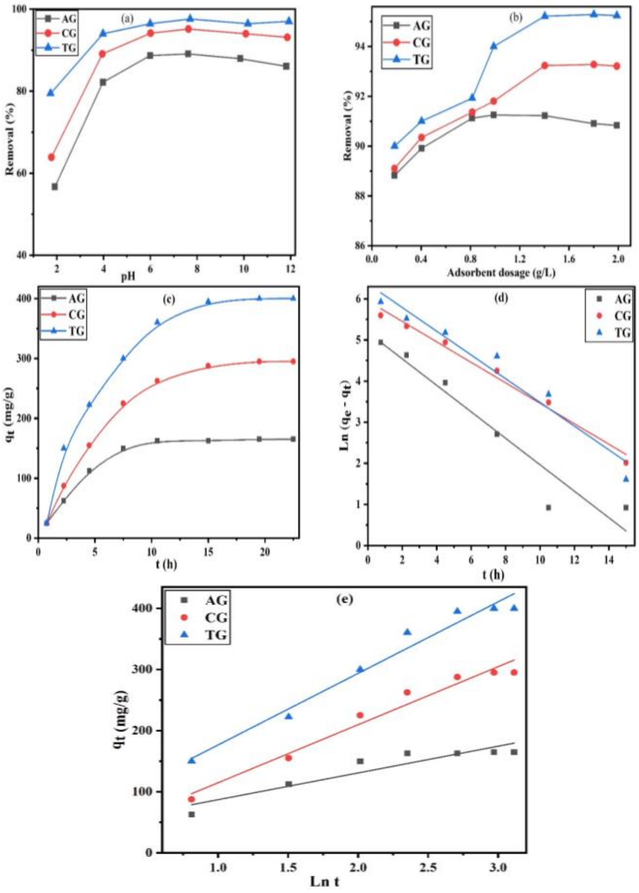

Fig. (3): (a) pH effect, (b) adsorbent dosage, (c) shaking time, (d) pseudo-first order kinetic, and (e) Elovich plots for MB adsorption onto AG, TG, and CG.

3.2.4. Effect of initial concentration of MB dye

Adsorption isotherm principles will be used to analyze how the initial concentration of MB affects the adsorption capacity (q_m, mg/g) of AG, NT, CF, TG, and CG samples. The adsorption of methylene blue at 17, 30, and 40 °C from solution at initial concentration (30–500 mg/L) keeping constant adsorbent dosage and pH values were discussed. Fig. (4, a-e) predicts that the adsorption of methylene blue is higher at the beginning of adsorption which may be related to the presence of higher free adsorption sites which acting as higher driving force to overcome all mass transfer resistance for the adsorption process, leading to easier capture of MB, while at higher MB concentration the removal percentage decreases might be due to the saturation of binding sites [65, 66]. Different adsorption isotherm models have been used as Langmuir (Eq. 11), Freundlich (Eq. 13), Temkin (Eq. 14), and Dubinin-Radushkevich (Eq. 16) isotherms have been tested as shown in Fig. (4, f-j) and Fig. (5, a-j), respectively while the calculated parameters are illustrated in Table (3) and Table (4). All these adsorption isotherms were applied onto AG, NT, CF, TG, and CG at 17, 30, and 40 °C.

Upon analysis data of Table (3) and Figure (4), we found that a high affinity between MB and solid materials surface and a good applicability of Langmuir adsorption model according to the high values of correlation coefficient (R^2, 0.9802 and 0.9979) at different temperatures for all the prepared solid [67]. The values of maximum adsorption capacity (q_m, mg/g) increase with the increase of temperature for all adsorbents, signifying an endothermic nature of the existing adsorption process [68]. Maximum Langmuir adsorption capacities (q_m, mg/g) for AG, NT, CF, TG, and CG are 211.86, 88.62, 62.34, 448.76, and 330.25 mg/g, respectively at 40 ^{o}C where TG > CG > AG > NT > CF which may be related to the higher S_{BET} (m^2/g), V_T (cm^3/g), and the occurrence of new chemical functional groups for TG and CG. It is also noted that Langmuir constants (b, L/mg) for TG and CG (0.0215−0.1015) are the maximum values which represents on the strong attractions between solid surface and MB ions. The dimensionless parameter (R_L, Eq. 12) ranged between 0.0094 to 0.3964 for the adsorption of MB onto all the investigated solid adsorbents at all the applied temperature which is consistent with favorable adsorption.

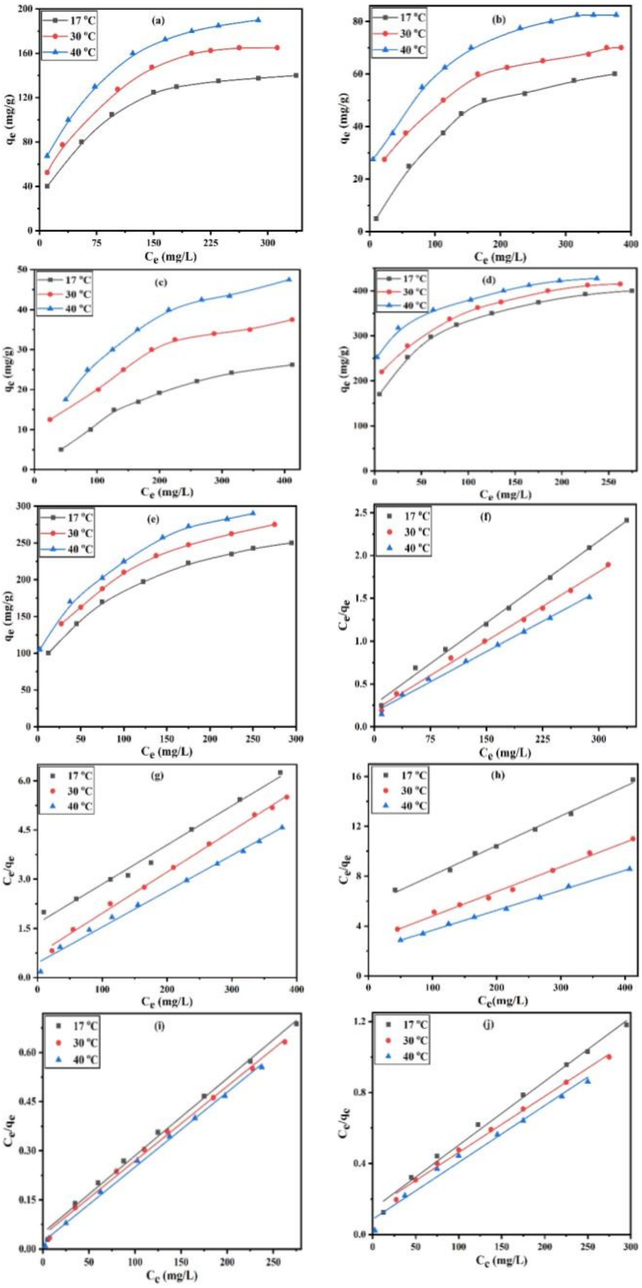

Fig. (4): Methylene blue adsorption isotherms (a-e) and plots of Langmuir model (f-j) for AG, NT, CF, TG, and CG at 17, 30, and 40 °C.

The obtained parameters from Freundlich plots are collected in Table (3). The observed R^2 is very close to unit indicates a good applicability of linear Freundlich adsorption equation. It is observed that K_F values increase with temperature for every solid adsorbent indicating the favorable adsorption process with heating. The *1/n* has a value between 0−1, illustrates that a strong interaction between MB$^+$ and adsorbents and the adsorption process is favorable on solid adsorbents [46].

Table (2): PFO, PSO, intra-particle diffusion, Elovich kinetic models, and the parameters of thermodynamic studies for adsorption of MB on CF, NT, AG, CG, and TG.

Models	Parameters	Temp.	CF	NT	AG	CG	TG
	q_m (mg/g)		------	------	185.87	315.46	438.60
PFO	q_{exp} (mg/g)		------	------	178.70	338.51	448.79
	k_1 (h^{-1})		------	------	0.3220	0.2490	0.2885
	R^2		------	------	0.9080	0.9818	0.9440
PSO	q_{exp} (mg/g)		------	------	191.41	400.31	485.85
	k_2 $\times 10^{-3}$ (g/mg.h)		------	------	1.231	0.253	0.390
	R^2		------	------	0.9789	0.9392	0.9907
Elovich	α (mg/g.h)		------	------	117.64	116.90	194.50
	β (g/mg)		------	------	0.0228	0.0105	0.0085
	R^2		------	------	0.8466	0.9600	0.9624
Intra-particle diffusion	k_o (mg/g. $h^{1/2}$)		------	------	42.850	75.465	100.048
	C		------	------	14.533	6.607	20.022
	R^2		------	------	0.8100	0.9200	0.9517
Thermo-dynamicParameters	R^2		0.9961	0.9361	0.9566	0.9985	0.9531
	ΔH^o (kJ/mol)		33.657	23.902	11.452	5.727	5.254
	ΔS^o (kJ/mol.K)		0.103	0.081	0.048	0.032	0.037
	$-\Delta G^o$ (kJ/mol)	17 °C	-3.743	0.538	2.575	3.644	5.532
		30 °C	-2.448	0.781	3.096	4.054	5.963
		40 °C	-1.418	1.282	3.701	4.388	6.393

Table (3): Freundlich and Langmuir adsorption parameters for MB on CF, NT, AG, TG, and CG at 17, 30, and 40 °C.

Models		**Langmuir**				**Freundlich**		
Parameters		**q_m (mg/g)**	**b (L/mg)**	**R_L**	**R^2**	**1/n**	**K_F**	**R^2**
Samples	**Temp.**							
CF	**17 °C**	42.09	0.0042	0.3964	0.9944	0.6512	0.580	0.9726
	30 °C	50.76	0.0070	0.2884	0.9910	0.5174	1.818	0.9571
	40 °C	62.34	0.0078	0.2439	0.9979	0.4738	2.960	0.9703
NT	**17 °C**	80.33	0.0075	0.2832	0.9869	0.4660	4.091	0.9242
	30 °C	81.33	0.0174	0.1026	0.9967	0.3411	9.726	0.9814
	40 °C	88.62	0.0252	0.0760	0.9907	0.3531	11.278	0.9733
AG	**17 °C**	157.23	0.0244	0.0679	0.9956	0.3685	18.142	0.9698
	30 °C	185.87	0.0274	0.0576	0.9955	0.3528	23.778	0.9845
	40 °C	211.86	0.0278	0.0565	0.9936	0.3233	32.118	0.9900
CG	**17 °C**	277.78	0.0215	0.0514	0.9911	0.2991	46.443	0.9963
	30 °C	315.46	0.0223	0.0576	0.9951	0.3051	50.580	0.9934
	40 °C	330.25	0.0353	0.0348	0.9802	0.2257	81.413	0.9755
TG	**17 °C**	423.72	0.0478	0.0203	0.9944	0.2204	119.015	0.9950
	30 °C	438.60	0.0547	0.0171	0.9954	0.1876	148.288	0.9915
	40 °C	448.76	0.1015	0.0094	0.9964	0.1184	222.585	0.9906

Table (4): Dubinin-Radushkevich and Temkin parameters for MB adsorption on CF, NT, AG, TG, and CG at 17, 30, and 40 °C.

Models		**Temkin**			**Dubinin-Radushkevich**		
Parameters		**b_T (J/mol)**	**K_T (L/g)**	**R^2**	**q_{DR} (mg/g)**	**E_{DR} (kJ/mol)**	**R^2**
Samples	**Temp.**						
CF	**17 °C**	268.99	0.044	0.9910	28.50	0.0142	0.9858
	30 °C	211.82	0.060	0.9818	38.12	0.0195	0.9945
	40 °C	178.64	0.066	0.9944	47.15	0.0218	0.9878
NT	**17 °C**	139.16	0.089	0.9484	62.44	0.0216	0.9788
	30 °C	164.37	0.213	0.9456	71.15	0.0268	0.9745
	40 °C	134.55	0.248	0.9879	85.48	0.0286	0.9812
AG	**17 °C**	79.66	0.345	0.9775	142.73	0.0322	0.9969
	30 °C	70.07	0.371	0.9818	173.72	0.0312	0.9964
	40 °C	66.51	0.457	0.9774	197.13	0.0329	0.9802
CG	**17 °C**	40.50	0.231	0.9972	261.17	0.0264	0.9752
	30 °C	37.74	0.238	0.9964	291.48	0.0277	0.9592
	40 °C	35.19	0.258	0.9862	308.30	0.0304	0.9908
TG	**17 °C**	33.35	0.992	0.9955	415.68	0.0332	0.9824
	30 °C	35.84	1.523	0.9948	430.62	0.0389	0.9665
	40 °C	51.43	19.920	0.9906	440.36	0.0468	0.9797

Temkin adsorption model of MB onto AG, NT, CF, TG, and CG is shown in Fig. (5, a-e) while Temkin parameters are listed in Table (4). The equilibrium binding constant values (K_T, L/g) increased with temperature for all the solid samples as shown in Table (4), demonstrating that endothermic adsorption is advantageous at higher temperatures [69]. Fig. (5, a-e) shows good linearity for Temkin isotherm where correlation coefficients (0.9456–0.9972) have high values. Temkin b_T values ranged from 33.35 to 268.99 J/mol ($b_T <$ 8 kJ/mol), indicating that MB adsorption is physisorption in nature at different temperatures [70].

Dubinin-Radushkevich model (DR) for MB adsorption on CF, NT, AG, TG, and CG at 17, 30, and 40 °C are shown in Fig. (5, f-j) and the calculated DR parameters are listed in Table (4). For all the examined substances at all applied temperatures, the difference between (q_{DR}, mg/g) and those calculated from Langmuir model (q_m, mg/g) ranged between 8.4–13.59%. The value of mean free energy (E_{DR}) calculated from the Dubinin-Raduskevich model can be used for interpreting whether the adsorption process is physical or chemical. It is known that, $E_{DR} <$ 8.0 kJ/mol hints physisorption, whereas the value 8–16 kJ/mol is referred to chemisorption. In this work, E_{DR} is referred to physical adsorption process [61]. MB adsorption data is well fitted with Langmuir, Freundlich, Temkin, Dubinin-Radushkevich, endothermic and physical adsorption process according to all of the previous results.

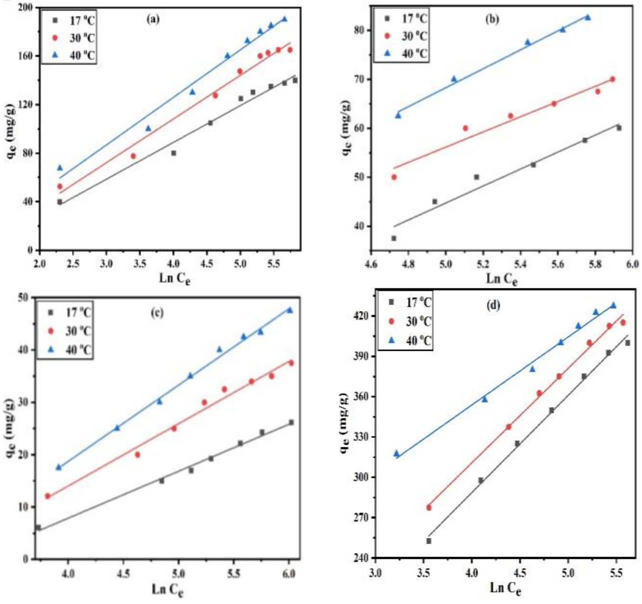

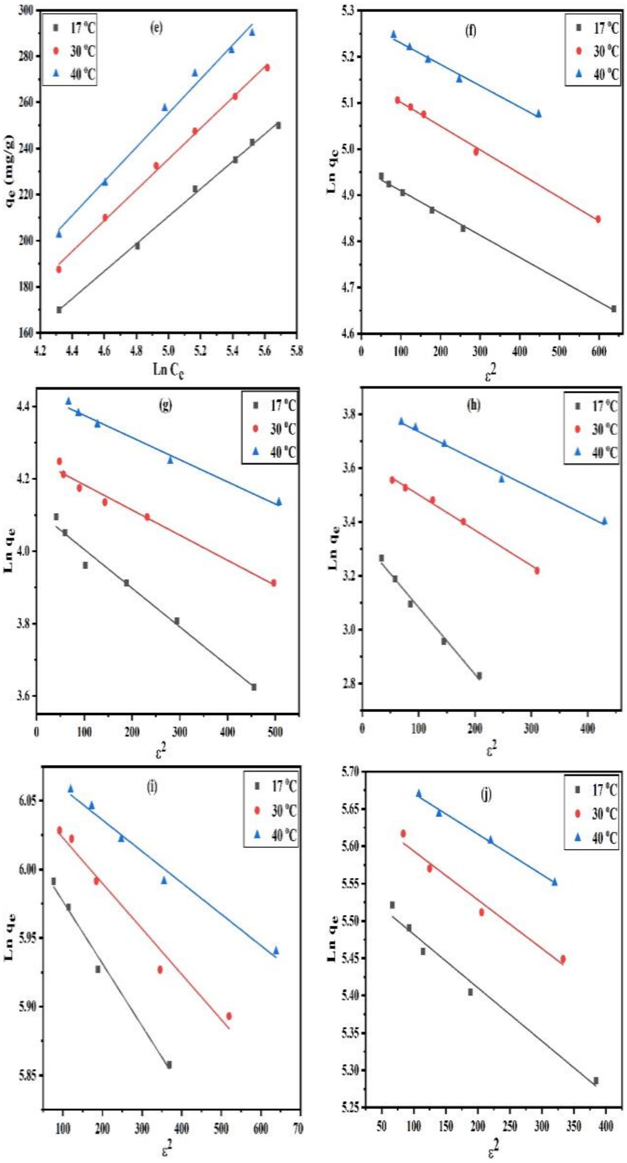

Fig. (5): Temkin (a-e) and linear DR plots (f-j) for MB adsorption onto AG, NT, CF, TG, and CG at 17, 30, and 40 °C.

3.2.5. Thermodynamic parameters

The effect of temperature change is related to three thermodynamic parameters namely the change in enthalpy ($\Delta H°$) and entropy ($\Delta S°$) which are calculated from the model of Van't Hoff (Eq. 20, Fig. (6)), while the change in free energy ($\Delta G°$) was calculated from Equation 21, and the values of parameters are summarized in Table (2). Upon inspection of the data in Table (2), (i) the higher correlation coefficients (R^2) values for Van't Hoff plot ranged between (0.9361–0.9985) prove the good fitting of Van't Hoff model. (ii) The negative values of free energy changes for all prepared samples except CF mean the spontaneous adsorption process. (iii) The positive value of enthalpy change which ranged between 5.254–33.657 kJ/mol indicated endothermic nature of adsorption process. (iv) The positive value of standard entropy which ranged between 0.032–0.103 kJ/mol.K reflects the increased randomness at the interface between solid and solution surface [71]. (v) MB adsorption is a physical process as the calculated ΔG^o values are found < 5 kJ/mol for all samples (except TG). Moreover, the calculated ΔH^o values are < 40 kJ/mol which indicate the physisorption process of adsorption [58].

3.3. Desorption study

The efficiency of MB desorption from TG using various desorbing agents was calculated using Eq. 22 and displayed in Fig. (6). Desorption data indicate that ethanol is the most efficient desorption solution where efficiency of desorption for pure water, benzene, propanol, chloroform, and ethanol was found to be 8.41, 14.33, 32.33, 35.38, and 75.46%, respectively. As shown in Figure (6), the desorption efficiency of distilled water was very low and that is related to the low number of positively charged protons [72]. The highest desorption power of 75.46% was confirmed by using ethanol as it diffuses into the pores of adsorbent resulting in the increase in solubility of the dye [73].

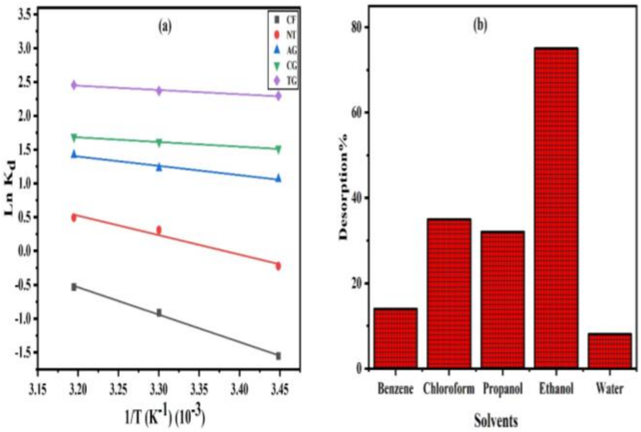

Fig. (6): (a) Van't Hoff plot for all the investigated adsorbents and (b) MB desorption from TG by applying various solvents.

3.4. Comparison of TG with other materials

In the present study, TG is compared with other materials Table (5) [62, 70, 74, 75]. The data represent the higher adsorption efficiency for titanium dioxide/calcium alginate composite (TG) as a promising solid adsorbent for the adsorption of methylene blue from an aqueous medium.

Table (5): Methylene blue maximum adsorption capacity using TG in comparison with othercomposites.

Solid materials	Maximum adsorption capacity	References
SC4	248.9 mg/g	[62]
Glutaraldehyde cross-linked alginate/sepiolite hydrogel capsules	294.1 mg/g	[70]
Magnetic biochar	129.61 mg/g	[74]
Agar/κ-carrageenan hydrogel	242.3 mg/g	[75]
TG	423.72 mg/g	[This study]

Conclusion

In this study, both of titanium dioxide/calcium alginate composite (TG) and cupper ferrite/calcium alginate composite (CG) were fabricated using nanotitania and cupper ferrite in the presence of calcium alginate as a biopolymer matrix structure. Thermal, textural, and chemical investigation techniques showed that the insertion of nanotitania and cupper ferrite into alginate (TG and CG, respectively) raise the textural and chemical properties of the formed composites. Where, S_{BET} for TG and CG is increased by nearly 4.0 and 1.5 times, respectively when NT and CF were mixed with the biopolymer matrix. TG exhibited the maximum adsorption capacity at 40 ^{o}C (q_m, 448.76 mg/g). Adsorption of MB onto TG and CG revealed that 1.4 g/L as adsorbent dosage, pH = 8, and 15 h as contact shaking time were the optimum adsorption conditions. The adsorption process follows Langmuir, Dubinin-Radushkevich, and Temkin adsorption models. Kinetic and thermodynamic parameters proved that the process is endothermic, spontaneous, and follows PFO model. Solid reusability is confirmed by ethanol as desorbing agent with 75.46% as desorption efficiency. The previous study confirms the feasibility of the fabricated TG and CG nanoparticles in environmental applications toward the removal of organic dyes.

4. References

1. Natarajan, S., Bajaj, H. C., Tayade, R. J. (2018) Recent advances based on the synergetic effect of adsorption for removal of dyes from waste water using

photocatalytic process. *Journal of Environmental Sciences*, **65**, 201–222.

2. Surolia, P. K., Tayade, R. J., Jasra, R. V. (2010) Photocatalytic degradation of nitrobenzene in an aqueous system by transition-metal-exchanged ETS-10 zeolites. Industrial & engineering chemistry research, **49(8)**, 3961–3966.
3. Kumar, A., Pandey, G. (2017) A review on the factors affecting the photocatalytic degradation of hazardous materials. *Mater. Sci. Eng. Int. J*, **1(3)**, 1–10.
4. Song, J., Zou, W., Bian, Y., Su, F., Han, R. (2011) Adsorption characteristics of methylene blue by peanut husk in batch and column modes. Desalination, **265**(1–3), 119–125.
5. Vimonses, V., Lei, S., Jin, B., Chow, C. W., Saint, C. (2009) Kinetic study and equilibrium isotherm analysis of Congo Red adsorption by clay materials. *Chemical Engineering Journal,* **148(2–3),** 354–364.
6. Gautam, P. K., Gautam, R. K., Banerjee, S., Lofrano, G., Sanroman, M. A., Chattopadhyaya, M. C., Pandey, J. D. (2015) Preparation of activated carbon from Alligator weed (Alternenthera philoxeroids) and its application for tartrazine removal: Isotherm, kinetics, and spectroscopic analysis. *Journal of Environmental Chemical Engineering***, 3(4),** 2560–2568.
7. Benkhaya, S., M'rabet, S., El Harfi, A. (2020) A review on classifications, recent synthesis and applications of textile dyes. Inorganic Chemistry Communications, **115**, 107891–107960.
8. Rawat, A. P., Kumar, V., Singh, D. P. (2020) A combined effect of adsorption and reduction potential of biochar derived from Mentha plant waste on removal of methylene blue dye from aqueous solution. Separation Science and Technology, **55(5),** 907–921.
9. Hassan, A. F., Abdel-Mohsen, A. M., Fouda, M. M. (2014) Comparative study of calcium alginate, activated carbon, and their composite beads on methylene blue adsorption. Carbohydrate polymers, **102**, 192–198.
10. Singha, N. R., Chattopadhyay, P. K., Dutta, A., Mahapatra, M., Deb, M. (2019) Review on additives-based structure-property alterations in dyeing of collagenic matrices. *Journal of Molecular Liquids*, **293**, 111470–111576.
11. Shi, P., Hu, X., Duan, M. (2021) A UIO-66/tannic acid/chitosan/polyether sulfone hybrid membrane-like adsorbent for the dynamic removal of dye and Cr (VI) from water. *Journal of Cleaner Production*, 290, 125794.
12. Cai, L., Ying, D., Liang, X., Zhu, M., Lin, X., Xu, Q., Cai, Z., Xu, X., Zhang, L. (2021) A novel cationic polyelectrolyte microsphere for ultrafast and ultra-efficient removal of heavy metal ions and dyes. *Chemical Engineering Journal***, 410,** 128404–128417.
13. Aziz, K. H. H., Miessner, H., Mueller, S., Mahyar, A., Kalass, D., Moeller, D., Khorshid, I., Rashid, M. A. M. (2018) Comparative study on 2, 4-dichlorophenoxyacetic acid and 2, 4-dichlorophenol removal from aqueous solutions via ozonation, photocatalysis and non-thermal plasma using a planar falling film reactor. *Journal of hazardous materials*, **343,** 107–115.
14. Li, Z., Wang, G., Zhai, K., He, C., Li, Q., Guo, P. (2018) Methylene blue adsorption from aqueous solution by loofah sponge-based porous carbons. Colloids and Surfaces A: Physicochemical and Engineering Aspects, **538**, 28–35.
15. Hernandez Martinez, H. (2018) Entrecruzamiento y descomposición térmica simultánea de grupos laterales para reducir el envejecimiento físico en membranas de poli (oxiindolebifenilileno) para separación de gases.
16. Salimi, F., Emami, S. S., Karami, C. (2018) Removal of methylene blue from water solution by modified nano-boehmite with Bismuth. Inorganic and Nano-Metal Chemistry, **48(1),** 31–40.
17. Wang, H., Shang, H., Sun, X., Hou, L., Wen, M., Qiao, Y. (2020) Preparation of thermo-sensitive surface ion-imprinted polymers based on multi-walled carbon nanotube composites for selective adsorption of lead (II) ion. Colloids and

Surfaces A: Physicochemical and Engineering Aspects**, 585**, 124139–124168.

18. Deng, F., Liang, J., Yang, G., Huang, Q., Dou, J., Chen, J., Wen, Y., Liu, M., Zhang, X., Wei, Y. (2021) Direct generation of poly (ionic liquids) on mesoporous carbon via Diels–Alder and multicomponent reactions for ultrafast adsorptive removal anionic organic dye with high efficiency. *Journal of Environmental Chemical Engineering***, 9(1),** 104872–104880.
19. Ahmadijokani, F., Mohammadkhani, R., Ahmadipouya, S., Shokrgozar, A., Rezakazemi, M., Molavi, H., Aminabhavi, T. M., Arjmand, M. (2020) Superior chemical stability of UiO-66 metal-organic frameworks (MOFs) for selective dye adsorption. *Chemical Engineering Journal*, **399**, 125346–125372.
20. Karthikeyan, P., Meenakshi, S. (2019) In-situ fabrication of cerium incorporated chitosan-β-cyclodextrin microspheres as an effective adsorbent for toxic anions removal. Environmental Nanotechnology, Monitoring & Management, **12**, 100272–100280.
21. Williams, D. (2008) The relationship between biomaterials and nanotechnology. *Biomaterials*, **29(12),** 1737–1738.
22. Husein, D. Z., Hassanien, R., Al-Hakkani, M. F. (2019) Green-synthesized cupper nano-adsorbent for the removal of pharmaceutical pollutants from real wastewater samples. Heliyon, **8(5),** e02339–e02347.
23. Yang, H., Yan, J., Lu, Z., Cheng, X., Tang, Y. (2009) Photocatalytic activity evaluation of tetragonal $CuFe_2O_4$ nanoparticles for the H_2 evolution under visible light irradiation. *Journal of Alloys and Compounds***, 476(1–2),** 715–719.
24. Huang, W., Zhu, J., Zeng, H. Z., Wei, X. H., Zhang, Y., Li, Y. R. (2006) Strain induced magnetic anisotropy in highly epitaxial $CoFe_2O_4$ thin films. Applied physics letters, **89(26),** 262506–262509.
25. Carey, M. J., Maat, S., Rice, P., Farrow, R. F. C., Marks, R. F., Kellock, A., Nguyen, P., Gurney, B. A. (2002) Spin valves using insulating cobalt ferrite exchange-spring pinning layers. Applied physics letters, **81(6),** 1044–1046.
26. Ashraf, M. A., Peng, W., Zare, Y., Rhee, K. Y. (2018) Effects of size and aggregation/agglomeration of nanoparticles on the interfacial/interphase properties and tensile strength of polymer nanocomposites. Nanoscale research letters, **13(1),** 1–7.
27. Hassan, A. F., Elhadidy, H., Abdel-Mohsen, A. M. (2017) Adsorption and photocatalytic detoxification of diazinon using iron and nanotitania modified activated carbons. *Journal of the Taiwan Institute of Chemical Engineers*, **75,** 299–306.
28. Tao, S., Gao, F., Liu, X., Sørensen, O. T. (2000) Preparation and gas-sensing properties of $CuFe_2O_4$ at reduced temperature. Materials Science and Engineering: B, **77(2),** 172–176.
29. Isik, Z., Bilici, Z., Adiguzel, S. K., Yatmaz, H. C., Dizge, N. (2019) Entrapment of TiO_2 and ZnO powders in alginate beads: Photocatalytic and reuse efficiencies for dye solutions and toxicity effect for DNA damage. Environmental Technology & Innovation, **14**, 100358–100384.
30. Halomoan, I., Yulizar, Y., Surya, R. M., Apriandanu, D. O. B. (2022) Facile preparation of $CuO-Gd_2Ti_2O_7$ using Acmella uliginosa leaf extract for photocatalytic degradation of malachite green. Materials Research Bulletin, **150**, 111726–111736.
31. Viscusi, G., Lamberti, E., Gorrasi, G. (2022) Design of a hybrid bio-adsorbent based on Sodium Alginate/ Halloysite/ Hemp hurd for methylene blue dye removal: kinetic studies and mathematical modeling. Colloids and Surfaces A: Physicochemical and Engineering Aspects, **633**, 127925–127938.
32. Mahreni, M., Ramadhan, R. R., Pramadhana, M. F., Permatasari, A. P., Kurniawati, D., Kusuma, H. S. (2022) Synthesis of Metal Organic Framework (MOF) based Ca-Alginate for adsorption of malachite green dye. Polymer Bulletin, **5**, 1–15.
33. Lagergren, S. (1898) About the theory of so-called adsorption of solution

substances. Sven Vetenskapsakad Handingarl, **24(4),** 1–39.

34. Jasper, E. E., Ajibola, V. O., Onwuka, J. C., (2020) Non-linear regression analysis of the sorption of crystal violet and methylene blue from aqueous solutions onto an agrowaste derived activated carbon. Applied Water Science, **10 (6),** 1–11.
35. Weber W., Morris J. (1963) Kinetics of adsorption on carbon from solution. *Journal of the Sanitary Engineering Division by American Society of Civil Engineers*, **89**, 31–60.
36. Jayalakshmi, R., Jeyanthi, J., Sidhaarth, K. A. (2022) Versatile application of cobalt ferrite nanoparticles for the removal of heavy metals and dyes from aqueous solution. Environmental Nanotechnology, Monitoring & Management, **17**, 100659–100674.
37. Langmuir, I. (1918) The adsorption of gases on plane surfaces of glass, mica, and platinum. *Journal of the American Chemical society*, **40(9),** 1361–1403.
38. Freundlich, H. M. F. (1906) Over the adsorption in solution. *J. Phys. chem*, **57(385471),** 1100–1107.
39. Temkin, M. J., Pyzhev, V. (1940) Recent modifications to Langmuir isotherms. Acta Phys chim USSR, **12(1)**, 217–222.
40. Dubinin, M. M., Radushkevich, L. V. (1947) Equation of the characteristic curve of activated charcoal. Proc Acad Sci USSR Phys Chem Sect, **55**, 331–333.
41. Wang, B., Wang, Y., Wang, S. (2021) Improved water pollution index for determining spatiotemporal water quality dynamics: Case study in the Erdao Songhua River Basin, China. Ecological Indicators, **129**, 107931–107942.
42. Teodoro, F. S., Elias, M. M. C., Ferreira, G. M. D., Adarme, O. F. H., Savedra, R. M. L., Siqueira, M. F., da Silva, L. H. M., Gil, L. F., Gurgel, L. V. A. (2018) Synthesis and application of a new carboxylated cellulose derivative. Part III: Removal of auramine-O and safranin-T from mono-and bi-component spiked aqueous solutions. *Journal of colloid and interface science*, **512**, 575–590.
43. Hu, Z. P., Jiang, H. L., Hu, Q. D., He, F. A., Zou, H. L., Zhong, Z. R., Zhu, Q. J., Lv, H. W., Yang, Y. Y. (2022) Preparation of the hexachloro cyclo triphosphazene crosslinked sodium alginate polymer/multi-walled carbon nanotubes composite powder for the removal of the cationic dyes. *Journal of Molecular Structure*, **1262**, 133050–133064.
44. Nasef, M. M., Saidi, H. (2000) Thermal degradation behavior of radiation grafted FEP-g-polystyrene sulfonic acid membranes. Polymer degradation and stability, **70(3),** 497–504.
45. Jwo, C. S., Chang, H., Kao, M. J., Lin, C. H. (2007) Photodecomposition of volatile organic compounds using TiO_2 nanoparticles. *Journal of Nanoscience and Nanotechnology*, **7(6),** 1947–1952.
46. Zheng, X. M., Dou, J. F., Xia, M., Ding, A. Z. (2017) Ammonium-pillared montmorillonite-$CoFe_2O_4$ composite caged in calcium alginate beads for the removal of Cs^+ from wastewater. Carbohydrate polymers, **167**, 306–316.
47. Zhang, W., Tao, Y., Li, C. (2018) Sol-gel synthesis of Gd_2Ti_2O7/HZSM-5 composite photocatalyst for ofloxacin degradation. *Journal of Photochemistry and Photobiology A: Chemistry*, **364**, 787–793.
48. Sundarrajan, P., Eswaran, P., Marimuthu, A., Subhadra, L. B., Kannaiyan, P. (2012) One pot synthesis and characterization of alginate stabilized semiconductor nanoparticles. Bulletin of the Korean Chemical Society, **33(10)**, 3218–3224.
49. Diantoro, M., Kusumaatmaja, A., Triyana, K. (2018) Study on photocatalytic properties of TiO_2 nanoparticle in various pH condition. *Journal of Physics: Conference Series. IOP Publishing*, **1011(1)**, 012069–012076.
50. Ahmed, M. A., El-Katori, E. E., Gharni, Z. H. (2013) Photocatalytic degradation of methylene blue dye using Fe_2O_3/TiO_2 nanoparticles prepared by sol–gel method. *Journal of Alloys and Compounds*, **553**, 19–29.
51. Jayalakshmi, R., Jeyanthi, J. (2021) Spectroscopic investigation of carbon

nanotube as nano-filler entrapped in chitosan hydrogel beads. *Journal of Molecular Structure*, **1237**, 130386–130395.

52. Majnis, M. F., Yee, O. C., Adnan, M. A. M., Hamid, M. R. Y., Shaari, K. Z. K., Julkapli, N. M. (2022) Photoactive of Chitosan-ZrO_2/TiO_2 thin film in catalytic degradation of malachite green dyes by solar light. Optical Materials, **124**, 111967–111978.
53. Houšková, V., Štengl, V., Bakardjieva, S., Murafa, N. (2008) Photoactive materials prepared by homogeneous hydrolysis with thioacetamide: Part 2—TiO_2/ZnO nanocomposites. *Journal of Physics and Chemistry of solids*, **69(7)**, 1623–1631.
54. Iqbal, J., Shah, N. S., Sayed, M., Imran, M., Muhammad, N., Howari, F. M., Alkhoori, S. A., Khan, J. A., Bhatnagar, A., Haija, M. A., et. al. (2019) Synergistic effects of activated carbon and nano-zerovalent cupper on the performance of hydroxyapatite-alginate beads for the removal of As^{3+} from aqueous solution. *Journal of Cleaner Production*, **235**, 875–886.
55. Manuja, A., Kumar, S., Dilbaghi, N., Bhanjana, G., Chopra, M., Kaur, H., Kaur, R., Manuja, B. K., Singh, S. K., Yadav, S. C. (2014) Quinapyramine sulfate-loaded sodium alginate nanoparticles show enhanced trypanocidal activity. Nanomedicine, **9(11)**, 1625–1634.
56. Larosa, C., Salerno, M., de Lima, J. S., Meri, R. M., da Silva, M. F., de Carvalho, L. B., Converti, A. (2018) Characterisation of bare and tannase-loaded calcium alginate beads by microscopic, thermogravimetric, FTIR and XRD analyses. *International journal of biological macromolecules*, **115**, 900–906.
57. Ghorai, T. K., Chakraborty, M., Pramanik, P. (2011) Photocatalytic performance of nano-photocatalyst from TiO_2 and Fe_2O_3 by mechanochemical synthesis. *Journal of Alloys and Compounds*, **509(32),** 8158–8164.
58. Kumar, M., Dosanjh, H. S., Singh, H. (2019) Biopolymer modified transition metal spinel ferrites for removal of fluoride ions from water. Environmental Nanotechnology, Monitoring & Management, **12**, 100237–100246.
59. Zhao, K., Feng, L., Li, Z., Fu, Y., Zhang, X., Wei, J., Wei, S. (2014) Preparation, characterization, and photocatalytic degradation properties of a TiO_2/calcium alginate composite film and the recovery of TiO_2 nanoparticles. RSC Advances, **4(93),** 51321–51329.
60. Matos, J., Marino, T., Molinari, R., García, H. (2012) Hydrogen photoproduction under visible irradiation of Au–TiO_2/activated carbon. Applied Catalysis A: General, **417**, 263–272.
61. Kooh, M. R. R., Thotagamuge, R., Chau, Y. F. C., Mahadi, A. H., Lim, C. M. (2022) Machine learning approaches to predict adsorption capacity of Azolla pinnata in the removal of methylene blue. *Journal of the Taiwan Institute of Chemical Engineers*, **132**, 104134–104140.
62. Grassi, P., Lunardi, P., Foletto, E. L., Dotto, G. L., Lima, E. C., Jahn, S. L. (2022) Production of sugar-derived carbons by different routes and their applications for dye removal in water. Chemical Engineering Research and Design, **182,** 237–245.
63. Badruddoza, A. Z. M., Hazel, G. S. S., Hidajat, K., Uddin, M. S. (2010) Synthesis of carboxymethyl-β-cyclodextrin conjugated magnetic nano-adsorbent for removal of methylene blue. Colloids and Surfaces A: Physicochemical and Engineering Aspects, **367(1–3)**, 85–95.
64. Walaa A. S., Grehan A. N., Ghada. E., Asaad F. H. (2022) Synthesis and characterization of ferric@nanocellulose/nanohydroxyapatite bio-composite based on sea scallop shells and cotton stalks: adsorption of Safranin-O dye, Biomass Conversion and Biorefinery.
65. Xu, S., Jin, Y., Li, R., Shan, M., Zhang, Y. (2022) Amidoxime modified polymers of intrinsic microporosity/alginate composite hydrogel beads for efficient adsorption of cationic dyes from aqueous solution. *Journal of Colloid and Interface Science*, **607**, 890–899.

66. Naiya, T. K., Bhattacharya, A. K., Mandal, S., Das, S. K. (2009) The sorption of lead (II) ions on rice husk ash. *Journal of hazardous materials*, **163(2–3),** 1254–1264.
67. Andronic, L., Isac, L., Cazan, C., Enesca, A. (2020) Simultaneous adsorption and photocatalysis processes based on ternary TiO_2–CuxS–fly ash hetero-structures. Applied Sciences, **10(22),** 8070–8085.
68. Mashkoor, F., Nasar, A., Jeong, C. (2022) Magnetized chitosan nanocomposite as an effective adsorbent for the removal of methylene blue and malachite green dyes. Biomass Conversion and Biorefinery**, 1**, 1–13.
69. Aljeboree, A. M., Alshirifi, A. N., Alkaim, A. F. (2017) Kinetics and equilibrium study for the adsorption of textile dyes on coconut shell activated carbon. *Arabian journal of chemistry*, **10**, S3381–S3393.
70. Parlayıcı, Ş. (2022) Green biosorbents based on glutaraldehyde cross-linked alginate/sepiolite hydrogel capsules for methylene blue, malachite green, and methyl violet removal. Polymer Bulletin, 1–27.
71. Egbedina, A. O., Adebowale, K. O., Olu-Owolabi, B. I., Unuabonah, E. I., Adeyemo, M. A. (2022) Microwave synthesized carbon materials as low-cost and efficient adsorbents for the removal of antibiotics in single and binary systems. *Arabian Journal for Science and Engineering*, **47(5),** 5755–5765.
72. Daneshvar, E., Vazirzadeh, A., Niazi, A., Kousha, M., Naushad, M., Bhatnagar, A. (2017) Desorption of methylene blue dye from brown macroalga: effects of operating parameters, isotherm study and kinetic modeling. *Journal of Cleaner Production*, **152**, 443–453.
73. Inbaraj, B. S., Sulochana, N. (2006) Use of jackfruit peel carbon (JPC) for adsorption of rhodamine-B, a basic dye from aqueous solution. *Ind. J. chem. Tech.*, **1**, 17–23.
74. Wen, Q., Chen, Y., Rao, X., Yang, R., Zhao, Y., Li, J., Xu, S., Liang, Z. (2022) Preparation of magnesium Ferrite-Doped magnetic biochar using potassium ferrate and seawater mineral at low temperature for removal of cationic pollutants. Bioresource Technology, **350**, 126860–126868.
75. Duman, O., Polat, T. G., Diker, C. Ö., Tunç, S. (2020) Agar/κ-carrageenan composite hydrogel adsorbent for the removal of methylene blue from water. *International journal of biological macromolecules*, 1**60**, 823–835.